



## Structural Architecture of the Hydrothermal System from Geophysical Data in Hammam Bouhadjar Area (Northwest of Algeria)

BOUALEM BOUYAHIAOUI,<sup>1</sup> ABDESLAM ABTOUT,<sup>1</sup> LAMINE HAMAI,<sup>1</sup> HASSINA BOUKERBOUT,<sup>1</sup> HAMOU DJELLIT,<sup>1</sup> SAID SOFIANE BOUGHICHE,<sup>1</sup> MOHAMED BENDALI,<sup>1</sup> and HAMZA BOUABDALLAH<sup>1,2</sup>

**Abstract**—We determine the structural architecture of the hydrothermal system of Hammam Bouhadjar area (Northwest of Algeria) by the use of geophysical data. New gravity and electrical surveys covered an area of about 48 km<sup>2</sup> in 2009. There were 350 gravity measurements made with a sampling of 500 m and 45 electrical soundings (Schlumberger type, AB = 1000 m). The Bouguer anomaly map shows a regression of gravity field towards the NW and SE. All of the observed anomalies are elongated in NE–SW direction. The results obtained from different processing methods (gradients, upward continuation, Euler deconvolution, wavelet transform and modelling) of gravity data were used to generate structural map of the studied area. The vertical and horizontal variations of resistivity confirm the presence of superficial and deeper faults system. Following the geophysical (gravity and electrical) analysis and modelling, we propose a model to explain the origin of the Hammam Bouhadjar thermal waters. We suggest that the hot spring water comes from an aquifer located in sandstones lenses in the Senono–Oligocene Tellian unit. Following the gravity modelling the aquifer is identified at about 800 m, the same depth where the geothermal gradient is insufficient to heat the water. In these circumstances, the aquifer is probably heated by volcanic processes connected with a hot compartment by faults and contacts affecting structures identified in depth. The presence of a conductor along of the horseshoe area suggests that the water percolates into this area and then is drained by the different accidents to invade the whole area.

**Key words:** Gravity anomaly, electrical resistivity, thermal water, deep structure, Hammam Bouhadjar, Northwest of Algeria.

### 1. Introduction

The Maghrebides part (external zones) of the peri-Mediterranean Alpine Belt includes about 1200 km-

long EW-trending magmatic lineaments that extend from Galite Island off the northern coast of Tunisia to Ras Tarf in Morocco (Abbassene et al. 2016). The southern Mediterranean Sea is bounded in northern Algeria by an Alpine orogenic belt resulting from the collision of drifting of continental fragments from Europe with the North African margin (Durand-Delga and Fontboté 1980; Bouillin 1986; Frizon de Lamotte et al. 2000; Bracène and Frizon de Lamotte 2002). Along this belt several hot springs were produced.

There are more than 200 hot springs in the northern part of Algeria. The most important one is located in the Northeast part, with the temperature ranging between 20 °C and 97 °C (Belhai et al. 2014). At the Northwest, the western Algerian hydrothermal system belongs to the occidental Tell of the external zones of the Alpine-Magrebides belt (Belhai et al. 2015). The most important geothermal areas of western Algeria are Hammam Bouhadjar, Hammam Bouhnia and Hammam Boughrara. In this work we focus on Hammam Bouhadjar's hydrothermal system, located at Ain Temouchent (Fig. 1). The tectonic characteristics, in Ain Temouchent area, correspond to thrust ruptures associated with NE–SW trending fold-related faults showing “en-echelon” right-stepping distribution (Meghraoui 1988; Benouar et al. 1994; Meghraoui and Doumaz 1996a).

The Hammam Bouhadjar's hydrothermal system is located in the narrow depression delineating the M'leta basin. It is known as a collapsed geological space, formed after the establishment of the Tellian napes, between the Oran coastal mountains in the North and the Tessala massif in the South (Fig. 1). Its history is related to tectonic structures post-napes,

<sup>1</sup> Centre de Recherche en Astronomie, Astrophysique et Géophysique (CRAAG), BP 63, 16340 Bouzaréah, Alger, Algérie. E-mail: b.bouyahiaoui@craag.dz; b.bouyahiaoui@yahoo.com

<sup>2</sup> GeoExplo, Cité 602 Iogements, Bât. SCB 12, N°06, Les Dunes, Chéraga, Alger, Algérie.

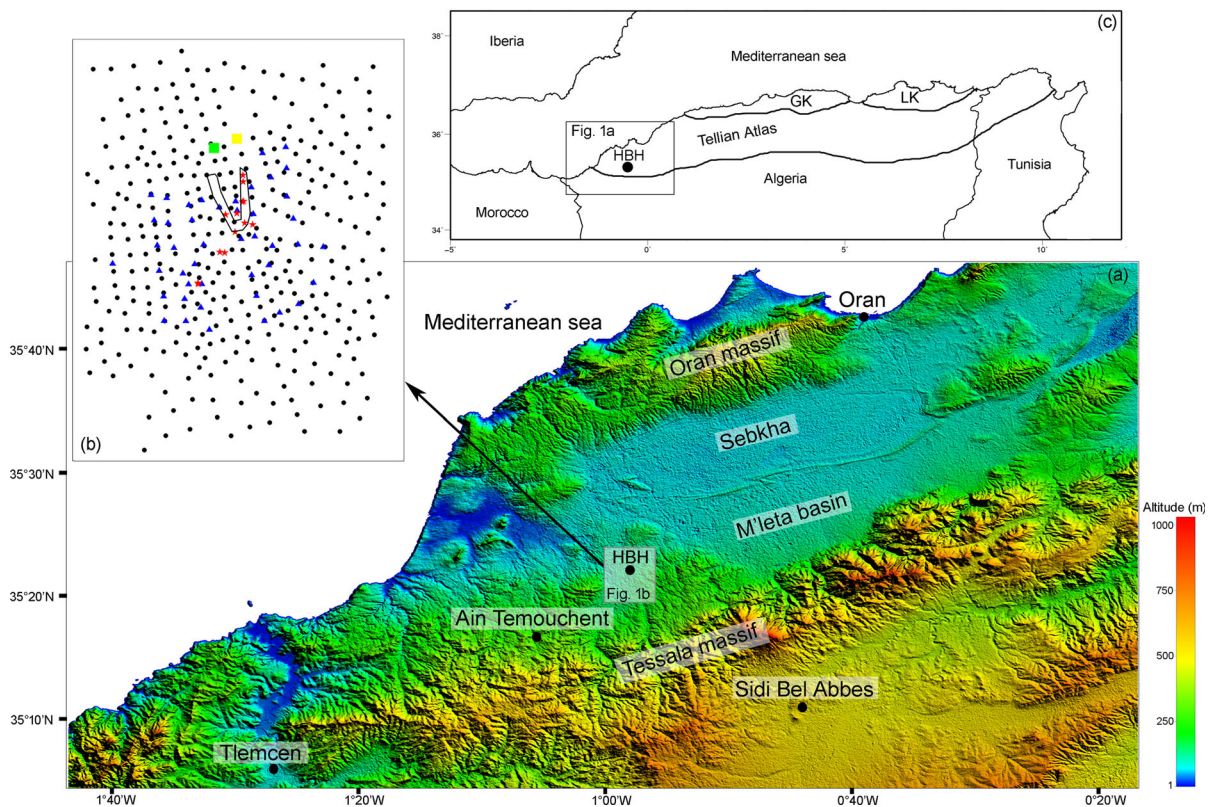


Figure 1

Location map of the studied area. **a** Superimposed on the topographic relief map from ETOPO1 1-min global relief ([www.ngdc.noaa.gov](http://www.ngdc.noaa.gov)). *Black rectangle* the area displayed in **(b)**. **b** The geophysical dataset used in this study. *Black circles* gravimetric measurements; *Green Square* absolute gravity reference; *Yellow Square* GPS reference; *Blue triangles* electrical soundings; *Red stars* hot springs and the *black line* shows the travertine deposits, drawing the “horseshoe”. **c** Overall position of the Hammam Bouhadjar area (Northwest Algeria)

essentially faults and volcanism, responsible of Neogene collapse that characterizes this region (Belhai et al. 2015). The thermal events, which are translated on the surface by low flow springs, are scattered on many points along the southern edge of the M'leta basin (Issaadi 1996). These thermal events follow NE–SW orientation and mark outstandingly the northern edge of Tessala massif further south.

We would like to understand the structural architecture of this hydrothermal system. To achieve this, we conducted geophysical surveys in Hammam Bouhadjar area to investigate and image it. The purpose was to bring elements of response to the following questions: is it a thermal fissure in connected with a draining and water circulation through tectonic contacts? How are they heated the latest and at what depth?

## 2. Geological Setting

The Tellian Atlas of Algeria underwent significant tectonics during the Cenozoic time. Neotectonic features correspond to E–W to NE–SW trending folds and reverse faults affecting Quaternary deposits (Meghraoui et al. 1996; Maouche et al. 2011). The western Algerian hydrothermal system belongs to the occidental Tell of the external zones of the Alpine-Magrebides belt (Belhai et al. 2014).

### 2.1. Geological Structure

The Hammam Bouhadjar geological structure consists of several structural units, tectonically superimposed. Above these units based thick post-napes accumulations, dating from the recent period

between the late Miocene and the Quaternary (late Serravallian to actually) (Perrodon 1957; Fenet 1975; Megartsi 1985). Schematically, this geological structure shows the following:

a parautochthonous Tellian substratum from Jurassic to Cretaceous can reach, locally, the antenapes Miocene, whose natures are limestone and dolomite (Perrodon 1957; Fenet 1975; Megartsi 1985; Louni-Hacini et al. 1995; Issaadi 1996). This parautochthonous unit defined significant potential reservoir that outcrops on the meridional front of Tellian napes, in the South of Sidi Bel Abbes. It also forms half-windows inside the M'leta basin in North of Ain Temouchent and Oran coastal massifs (Fig. 1).

Tellian napes units show heterogeneous allochthonous set made of marl-sandstone essentially and may contain few rare intercalations of reduced thickness of limestone (5–10 m), where are located small aquifers of reduced dimensions (Perrodon 1957; Fenet 1975; Megartsi 1985; Issaadi 1996). The Tellian napes occupy the middle of the M'leta basin. They correspond to series ranging from Vraconian to Oligocene and are represented by two sub-units: the first one from Vracono-Senonian and the second one from Senono-Oligocene (Issaadi 1996). These napes slipped by gravity during Miocene inside the same age deposits. Overall, the total thickness of allochthonous set composing these napes deposited during the Miocene is about 250 m, while, when slipping happened it was about 1200 m. The Tellian napes are visible in the Tessala massif until Ain Temouchent (Fig. 1).

Finally, at the top, Neogene post-napes deposits, whose potential aquifers are negligible and are located in surface. So they are too cold for being hot springs known in this area. These Neogene post-napes deposits cover the period from late Serravallian to actually (Perrodon 1957; Fenet 1975; Megartsi 1985; Louni-Hacini et al. 1995; Issaadi 1996). They are essentially outcropping in the Northern edge of the Tessala massif and inside the depression of M'leta (Fig. 1). This unit is crossed by volcanic bodies (dykes or sills), whose emplacement is spread over a period ranging from Miocene to Quaternary (Maury et al. 2000; Savelli 2002).

With these three structural and stratigraphic units, we noticed significant magmatic bodies. Their

geometry and outcropping ways suggest that the fissure volcanism was set up along Oued el Melah and Hammam Bouhadjar faults (Fenet 1975; Guardia 1975; Megartsi 1985; Louni-Hacini et al. 1995; Maury et al. 2000).

## 2.2. *Volcanism*

The apparent structural units (whatsoever the Tellian napes or the Neogene deposits) are crossed by volcanic bodies, deposited at relatively recent period, between 1.82 and 0.82 Ma (Louni-Hacini et al. 1995; Coulon et al. 2002; Belhai et al. 2015). The volcanism of Neogene age is characterized by the coexistence of two types of lavas: acid and basic. These ones are derived from two sources that authors (Louni-Hacini et al. 1995) associate to a subduction episode gradually evolving toward intraplate volcanism conditions, suggesting a magma percolation guided by tectonic fractures (Maury et al. 2000; Belhai et al. 2014). In plus, a part of Oran volcanism may be considered as a fissure volcanism which would be set up along deep accidents, affecting the crust, due to a distension phase, well known in this area at Neogene (Yelles-Chaouche et al. 2004). The numerous data show that the Oran region remains an active volcanic area until recent Quaternary (Belantour 2001). So, in these conditions, it appears clearly that the volcanic bodies which are located in the immediate vicinity of Hammam Bouhadjar and Ain Temouchent represent for some isolated or connected flows apophysis probably related to sufficiently deep hot chambers.

## 2.3. *Tectonic*

The major geological structure in Hammam Bouhadjar is the NNE–SSW fault that runs along the Eastern edge of Bled el Megane, seen near the Oued el Melah (Fig. 2). This fault, called the “Oued el Melah fault”, was well described by (Fenet 1975). It divided the area into two structural compartments: (i) at the West the raised structural compartment of Bled el Megane and (ii) at the East the fallen structural compartment of Hammam Bouhadjar, crossed by faults sub-system connected to the main fault (Fig. 2). This fault's sub-system is

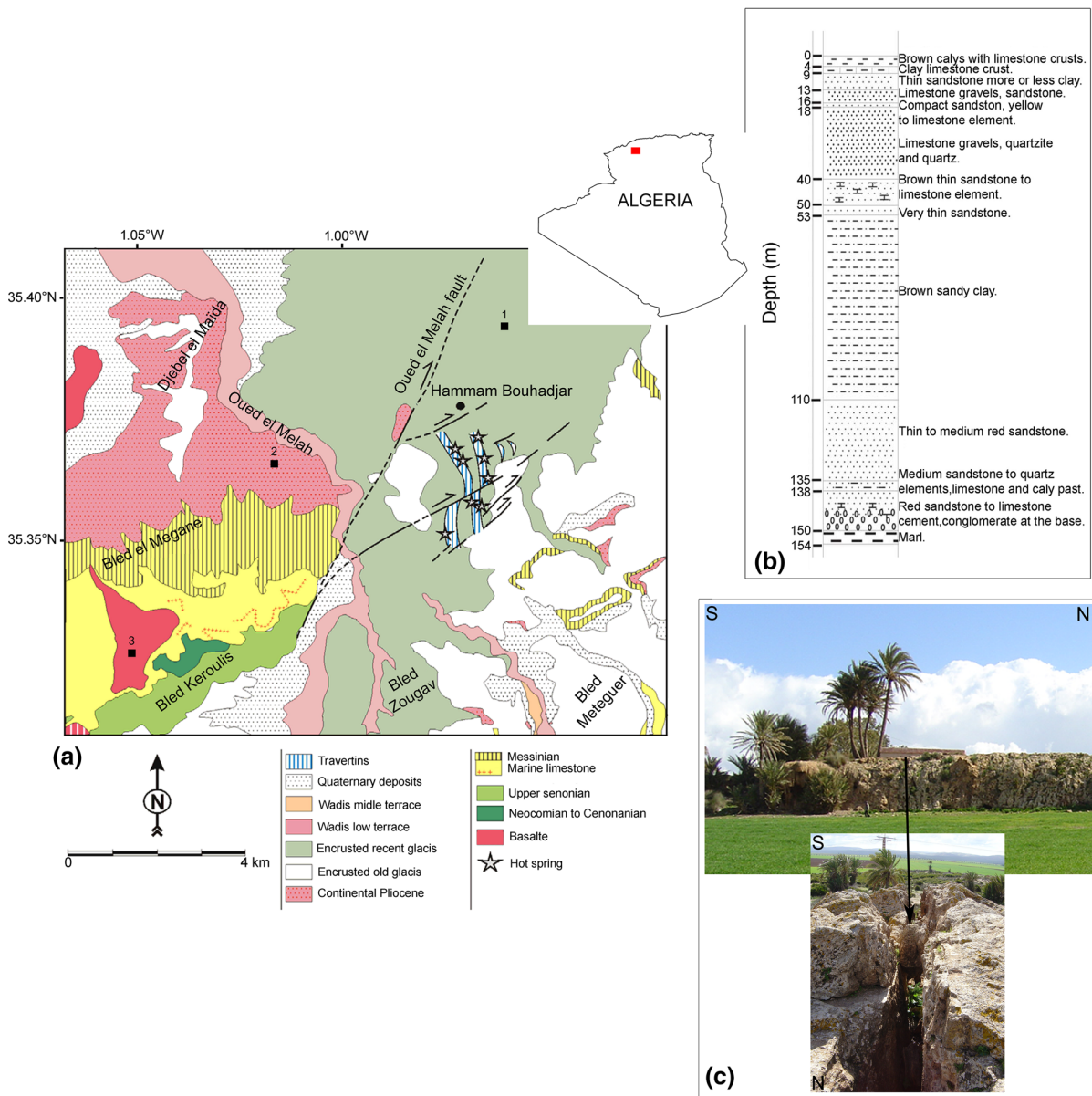


Figure 2

The geological map of Hammam Bouhadjar (according to the Ain Temouchent geological map, 1987). (1), (2) and (3) Represent the position of electrical calibration soundings in Hammam Bouhadjar drilling, on Pliocene formation and at the centre of volcanic emissions, respectively. Inset shows the global position of the study area (red square). **b** The different lithological formations of drilling Hammam Bouhadjar. **c** The travertine deposits forming the “horseshoe”

dipping from SW toward NE. From structural markers of deformation near Hammam Bouhadjar and along the North piedmont of Tessala massif, the determinate movements are clear and express a dextral transport associated with relative collapse of blocs.

The fault system that cut the Hammam Bouhadjar area is a textbook case. The “horseshoe”, along 800 m from 6 to 10 m of thickness, is produced by travertines deposits along open fractures whereby appear the thermal hot waters (Fig. 2c). It corresponds to tectonic slots filled of increasing



crystallisation fibre in the spreading direction of the fissure located in the slot centre (Fig. 2). In fact, the travertines deposits continue to the south of “horse-shoe”, and their detailed examination allows recognizing in the other side an accident headed N40. Another region, rich in hot springs is located at SW of this accident. The “horseshoe” slots of the NE area are shifted over about 500 m distance compared to those which extend to the south and located on the SW compartment.

### 3. Data Acquisition and Processing

#### 3.1. Gravimetric Prospecting

The gravimetric measurements were acquired in 2009, using a terrestrial Scintrex CG3 gravimeter. A total of 350 gravity measurements, spaced by ~500 m, covering an area of ~48 km<sup>2</sup> were measured (black circles, Fig. 1b). These data were tied to absolute gravity via a reference point situated in the studied area (green square, Fig. 1b). To perform the topographical corrections we determined the topographic coordinates of each measuring point using a bi-frequency differential GPS, Ashtech-Z12.

For quality control measures, we took the values of 16 stations. More than 90% of GPS reproduction points have less than 3 cm difference in altitude determination (Fig. 3a), while the distribution of the difference between two measurements at the same point presents a Gaussian shape, located at about 20 microgals (Fig. 3b).

The key document in the gravimetric survey is represented by complete Bouguer gravity anomaly, whose values are calculated by the following relationship:

$$g_b = g_{\text{obs}} - g(\varphi) + (0.3086h_s) - (0.0419d.h_s) + g_T,$$

where  $g_{\text{obs}}$  is the station observed gravity (in mgals),  $g(\varphi)$  represents the theoretical gravity calculated within the IUGG1967 system,  $h_s$  is the station elevation (in metres),  $d$  represents the density correction and  $g_T$  is the topographic corrections.

The Bouguer anomaly map (Fig. 4) is drawn from a regular grid of the Bouguer anomaly values

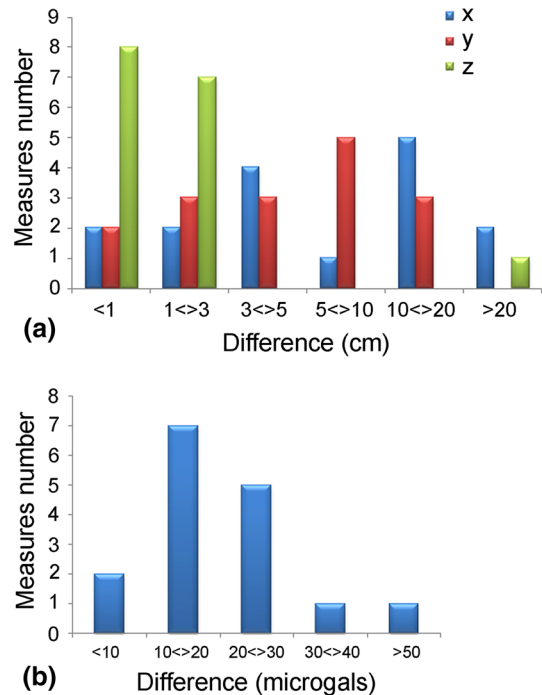


Figure 3

The histogram of cumulative frequency of standard deviation to reiterations. **a** GPS measures number of reproduction according to difference between the two measurements (blue, red and green for x, y and z, respectively). **b** Difference between two gravity measurements at the same point

obtained by interpolation using the minimum curvature method. A good representation of gravity data based on composite maps, in which are superimposed the image colour that reflects the spatial distribution of anomalies and shaded relief image, often in grey. This representation accentuates the gravimetric structures signatures perpendicular to the shading direction, allowing a qualitative visual interpretation, both structural and lithological (Fig. 4).

The Bouguer anomaly calculated includes all effects in the vertical direction (superficial, intermediate and deep). Therefore, it is necessary to process the Bouguer anomaly values to separate the different effects. To eliminate the regional effect (regional anomalies) and keep only the local anomalies (residual), we proceed to the separation by the polynomial method at different orders (Oldham and Sutherland 1955). Contrarily, for filtering the high-frequencies (short wavelengths), we applied the upward continuation, to move away high frequencies and eliminate

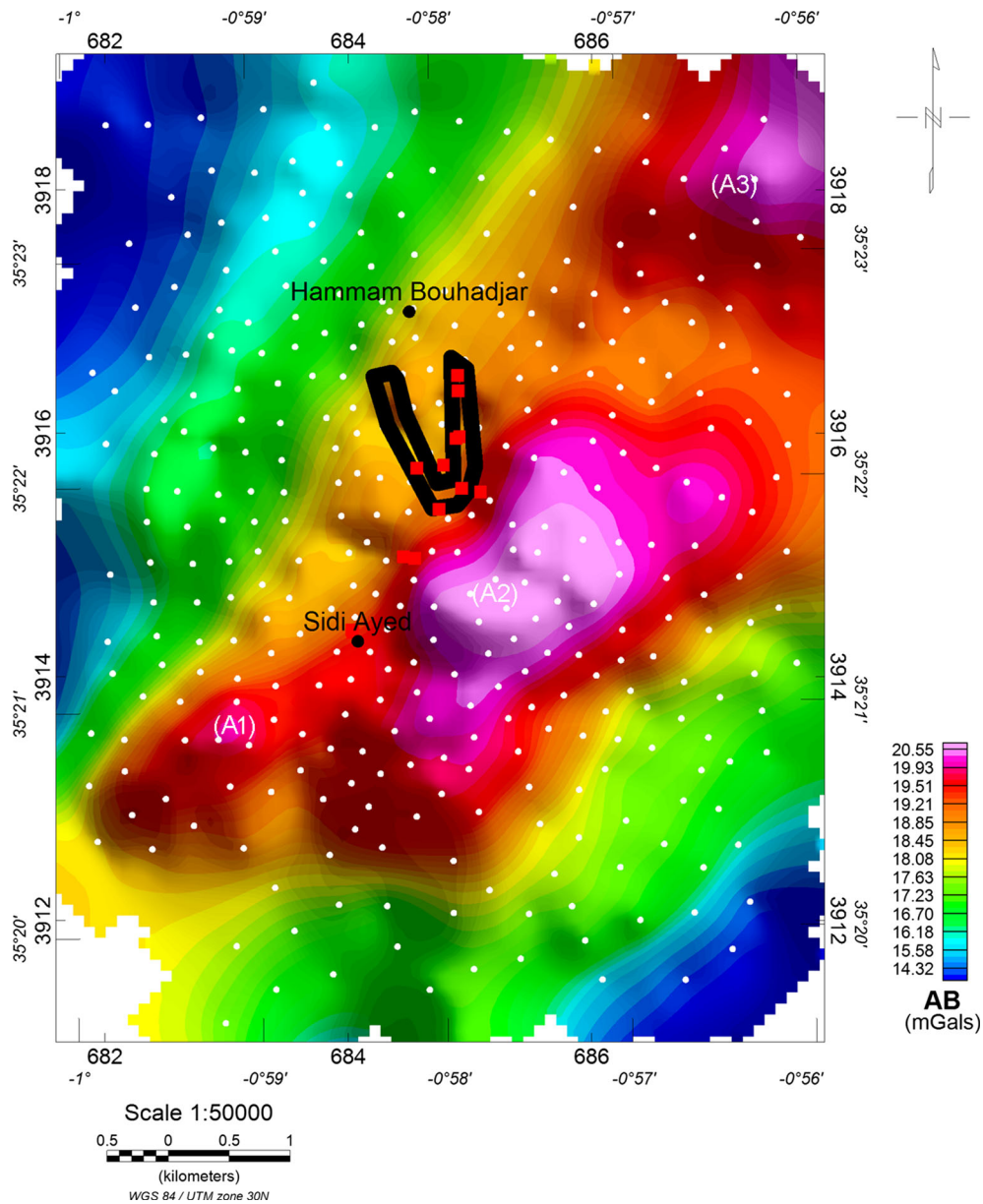


Figure 4

The Bouguer anomaly map of Hammam Bouhadjar area. The data were uniformly reduced with a density of  $2400 \text{ kg/m}^3$  for the Bouguer correction which is the mean density of the deposit formations ranging from Miocene to quaternary (Abtout et al. 2014). White circles correspond to gravimetric measurements; red squares represent hot springs and the black line shows the travertine deposits, drawing the "horseshoe"

the noise. We calculated upward continuations at several heights (more than 20), every 100 m (100, 200, 300...).

For better identification of generating sources of anomalies, we applied to the Bouguer anomaly a

specific processing, which is gradients filter: vertical and horizontal (Baranov 1953).

To better characterize anomalies and tectonic lineaments of the Hammam Bouhadjar area, we applied the Euler deconvolution (Thompson 1982;

Reid et al. 1990; Mikhailov et al. 2003) to gravity data. This method allows estimating the source depth automatically from the potential field data. It is based on the Euler's homogeneity equation which uses the horizontal and vertical gradients measured or calculated from the data. In addition to the depth, Euler deconvolution provides an indication of the source type with the structural index. We performed several tests by varying different parameters for structural index, window size and tolerance. The Euler solutions are well organized by using a structural index of 0, a window size equal to 12 and 15% of tolerance as parameters.

### 3.2. Electrical Prospecting

Forty-five electrical soundings (Schlumberger type, AB = 1000 m) were acquired (blue triangles, Fig. 1b). The material used is a SYSCAL R2 (Iris Instruments) with 250 W converter and 800 V maximum voltage. The measured values include all effects of crossed structures by the electric current, and the measured resistivity is called "apparent" (Keller 1966), given by the expression:  $K * \frac{\Delta V}{I}$  (where  $K$  represents geometrical constant). This apparent resistivity is converted to real resistivity by inversion process (Loke and Barker 1996). The interpretation of soundings curves was performed by using the "IPI2win" software, elaborated by Moscow State University. It is represented as table showing the real resistivity and thickness for each crossed layer.

We started by three calibration soundings, respectively, located as follows: (1) at one hundred metres of Hammam Bouhadjar drilling (see lithological column of this drilling, Fig. 2b), (2) on the Pliocene formation, situated at the west of the Hammam Bouhadjar faults and (3) at the centre of volcanic emissions (Fig. 2a).

## 4. Results

### 4.1. Sharp Density Contrast

The Bouguer anomaly map shows values ranging from +14.11 to +20.82 mGals (Fig. 4). The central part of this map is characterized by a set of positive anomalies (red colour, Fig. 4), consisting of three anomalies: (A1)

the first one, the short-wavelength anomaly, oriented NE–SW with a values of about +19.80 mGals, (A2) the second one, the long-wavelength anomaly, which extends over more than 3 km long, elongated NE–SW and showing higher values (+20.80 mGals) and finally, (A3) the beginning of the third positive anomaly which seems to continue in NE direction (Fig. 4). Geographically, the anomaly (A2) is located just south of horseshoe and hot springs. We will focus more particularly on this anomaly in the part dedicated to modelling. On both sides of this set of positive anomalies, the Bouguer anomaly values show a decay of gravity field toward the NW and SE (blue color, Fig. 4).

The residual anomaly map of order 1 (Fig. 5a) shows the position of relatively superficial gravity anomalies; it gives values of gravity field ranging between –2.00 and +4.20 mGals. This map presents the same trends found in the Bouguer anomaly map. Residual anomaly maps of order 2 and 3 (Fig. 5b, c) show the location of superficial gravity anomalies (the residual order 3 is more superficial than the residual order 2). A big lobe made of positive anomalies dominates almost all of these two maps (Fig. 5b, c). Moreover, compared to residual order 1 map, we notice the vanishing of the anomaly (A3).

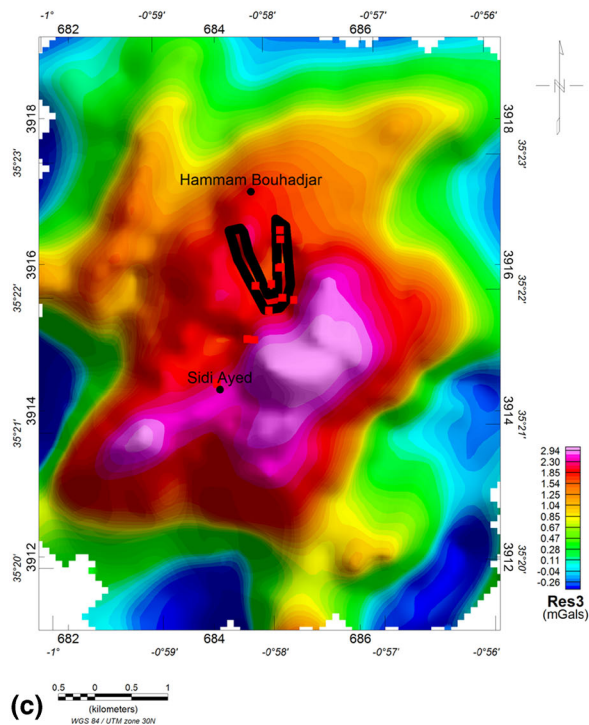
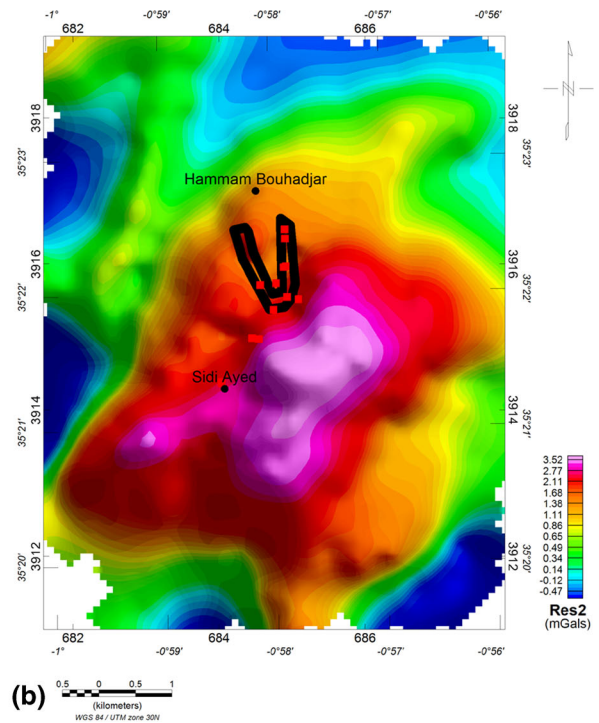
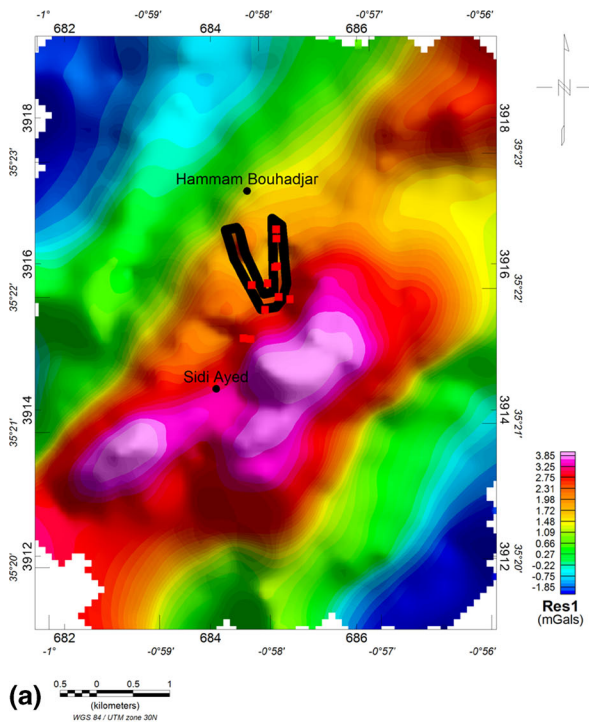
The vertical gradient map (Fig. 6) allows identifying area boundaries with different densities. On this map, the short wavelengths due to the initial noise are accentuated by the gradient filter. Essentially, we note in addition to the gravity lineaments separating A1, A2 and A3 anomalies, an axes sets with NE-SW trending separated by some NW–SE lineaments (Fig. 6).

Upward continuation at different altitudes allows attenuating local (superficial) anomalies and strengthening deep anomalies (Gibert and Galdeano 1985; Bouyahiaoui et al. 2011; Abtout et al. 2014). We publish in this paper upward continuation at 100, 500 and 1500 m (Fig. 7). These upward continuation maps show an attenuation of small anomalies to obtain a regular variation from 500 m (Fig. 7).

### 4.2. Deep Structures

#### 4.2.1 Energy Spectrum

The energy spectrum described by (Spector and Grant 1970) is written conventionally as the square of the



Fourier transform modulus of gravitational field. Slope of the logarithmic energy spectrum are proportional to the source depth, assuming that these

sources are statistically distributed near a horizontal level. It is mainly applicable for major depth estimating of sources set. Therefore, the anomalies



◀Figure 5

The residual maps of the Bouguer anomaly. **a**, **b** and **c** show the residual anomaly map of order 1, 2 and 3, respectively. The residual of order 3 shows more superficial anomalies. The map of residual of order 2 represents superficial structures than the map of residual of order 1. *Red squares* represent hot springs and the *black line* shows the travertines deposits, drawing the “horseshoe”

due to superficial sources (short wavelengths spectral content) and deep sources (large wavelengths spectral content) can be softly separated according to their spectral characteristics. Maximums and widths of the spectral amplitude are related to the depth and vertical extension of the disruptive body.

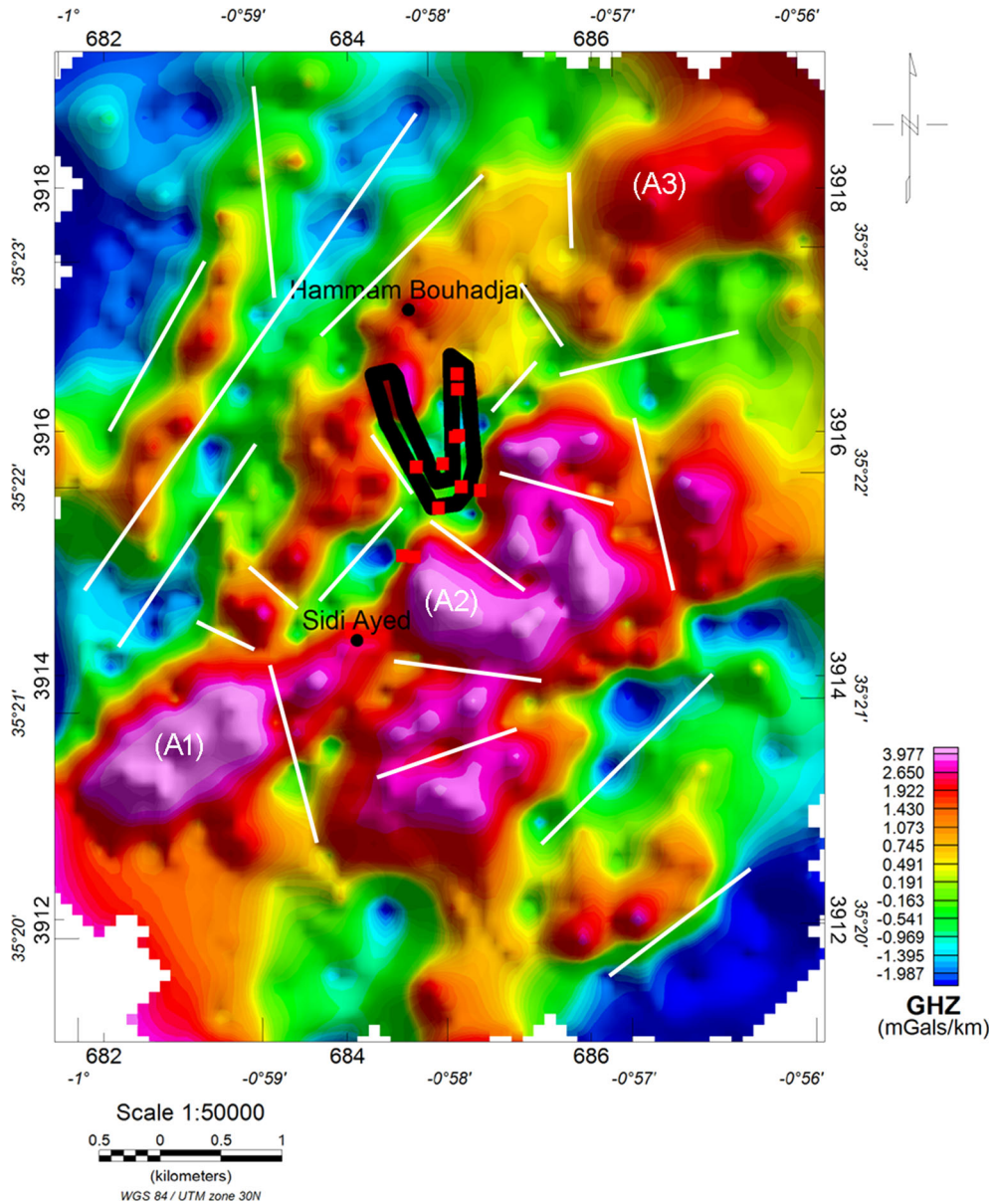


Figure 6

The vertical gradient map of the Bouguer anomaly. High-frequency anomalies visible in the Hammam Bouhadjar area correspond to faults and contacts (*white lines*). *Red squares* represent hot springs and the *black line* shows the travertine deposits, drawing the “horseshoe”

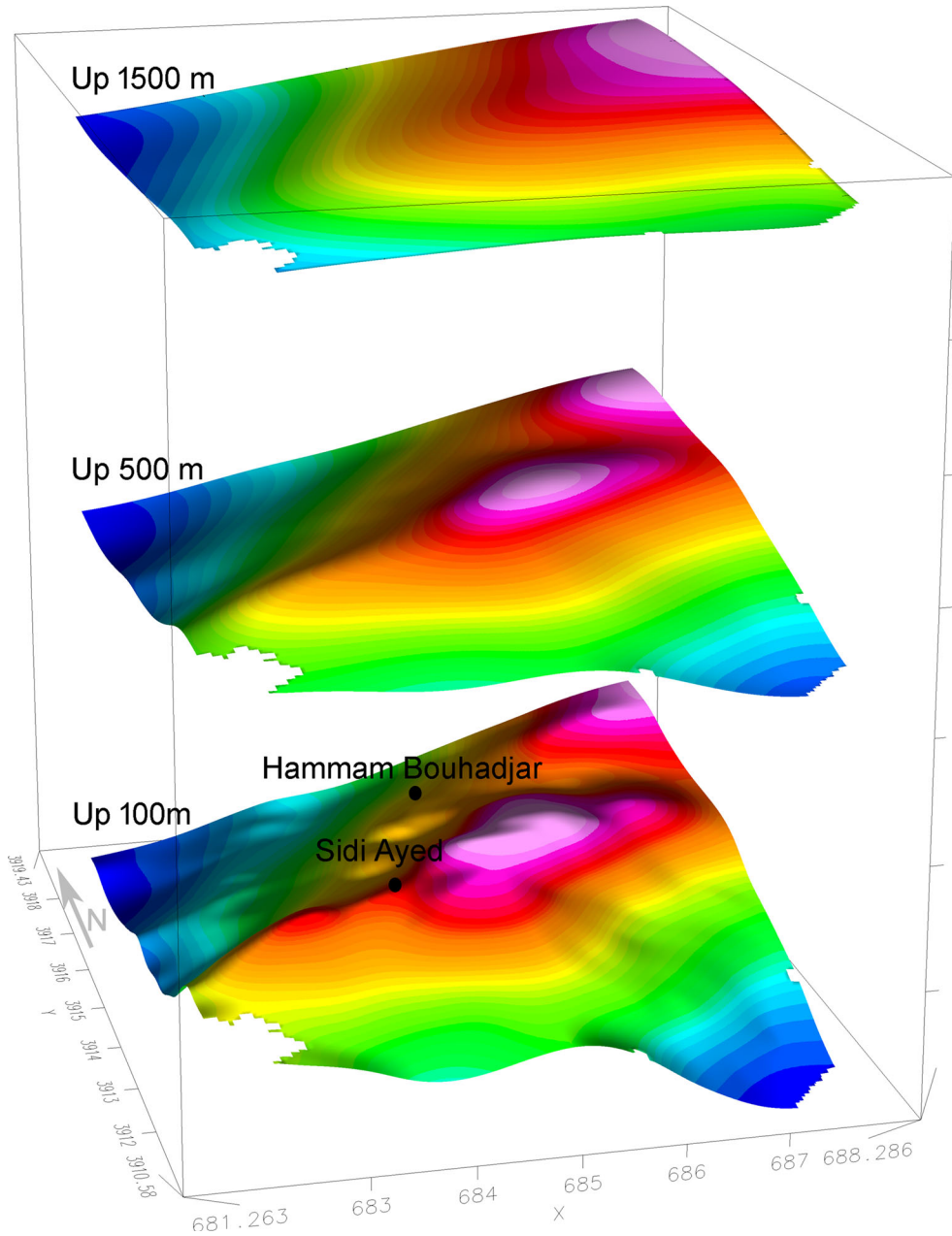


Figure 7  
Upward continuation at 100, 500 and 1500 m of the Bouguer anomaly maps

We used the curve representing signal energy according to the frequency after calculating the statistical mean of the spectral density of anomalies (Fig. 8). Thus, the depth pseudo “h” of the approximation plan is given by the following relation:

$$h = \Delta \log E / 4 * \pi * \Delta L,$$

where  $\Delta E$  is the log variation of the energy in  $\Delta L$  interval frequency.

We note the existence of two energy packets corresponding to the different wavelengths. The first

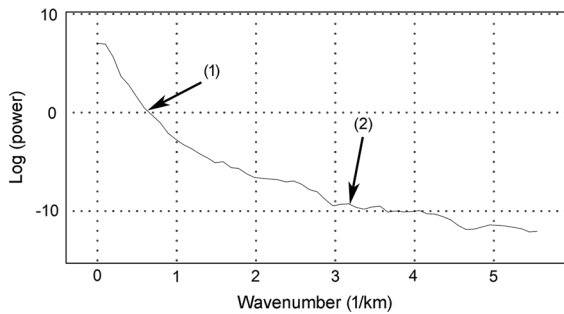


Figure 8

Energy spectrum of the Bouguer anomaly. It shows two energy packets with an estimated depth of about 800 m for the first one and 120 m for the second one

one represents the wavelengths  $>1000$  m, with an estimated depth at about 800 m and the second energy packet corresponds to short wavelengths, from 250 to 1000 m, giving a depth evaluated at about 120 m (Fig. 8).

#### 4.2.2 Euler Deconvolution

For a geological model such as an abnormal contact (Reid et al. 1990), we have chosen a window of 12 and 15% as tolerance. These parameters give Euler solutions with depth ranging between 100 and 700 m (Fig. 9). The positive anomalies set is bounded by two lineaments with NE–SW direction; the first one, located at the North, shows depth at about 400 m and greater depths ( $>600$  m) towards the northeast, while the second one, located at the South, is more shallow less than 250 m and deeper locally towards the northeast. Also, we note that the south of anomaly A2 is bounded by an E–W axis of about 500 m depth. Moreover, the two parts of negative anomalies, located at northwest and southeast, are delimited by two axes evaluated at more than 300 m of depth (Fig. 9).

#### 4.2.3 Identification of Anomalies Causative Bodies with the Continuous Wavelet Transform

We use the continuous wavelet transform method as described by many authors (such as Moreau et al. 1997; Hornby et al. 1999; Boukerbout et al. 2003; Fedi et al. 2004; Salliac et al. 2009 and so on) to localize the sources responsible of the anomalies. We apply this method on a profile trending in the

NW–SE direction (Fig. 10). This profile crosses the anomaly A2. The results obtained are shown in Fig. 10. The intensity of the complete Bouguer gravity anomaly varies from +14 to +20 mGals (top of Fig. 10). The wavelet coefficients of the continuous wavelet transform (middle of Fig. 10) shows the signature of two contacts or faults. Many contacts are identified but the more important are the one located in the NW part of the profile at a distance of about 0.6 km, and the second one identified in the maximum of the anomaly area at a distance of 5.4 km. The values of the maximum entropy criteria (bottom of Fig. 10) identify the depth of the top of the structures between 200 m and 1.6 km. The first contact is identified at a depth of about 700 m with entropy of 0.6 while the second one is identified at a depth of about 1.4 km with entropy of 0.7. These two contacts are overhanging structures located, respectively, at about 2.2 km and 1.8 km and identified with entropy of 0.8 and 0.9 and corresponding probably to apophysis connected to deep-rooted magma chamber.

### 4.3. Vertical and Horizontal Variations of Resistivity

#### 4.3.1 Calibration Sounding

The calibration sounding curves are shown in Fig. 11.

*Hammam Bouhadjar drilling* The high resistivity (350  $\Omega\cdot\text{m}$ ) of the first layer and its thinness (25 cm) is not characteristic of the formation. It is due mainly to the fact that the ground is relatively dry at the surface. Up to 2.75 m of depth, layers of medium resistivity are indicated (Fig. 11a). These layers correspond to sandstones (45  $\Omega\cdot\text{m}$ ) and clays (13  $\Omega\cdot\text{m}$ ). Between 2.75 m and 5.75 m of depth the limestone level is represented by a resistivity of 110  $\Omega\cdot\text{m}$ . Below, a thick layer ( $\sim 100$  m) with low resistivity (10.5  $\Omega\cdot\text{m}$ ) is well defined. Probably, it would correspond to the clays. It overcomes, clearly, a formation with 15.3  $\Omega\cdot\text{m}$  of resistivity which would be the sandstone aquifer level. All these results are well correlated with the drilling (Fig. 2b), except for formations ranging from 5.75 to 50 m of depth. Probably the gravel reported in the drilling has a clay matrix (highly conductive) more developed at the electrical sounding.



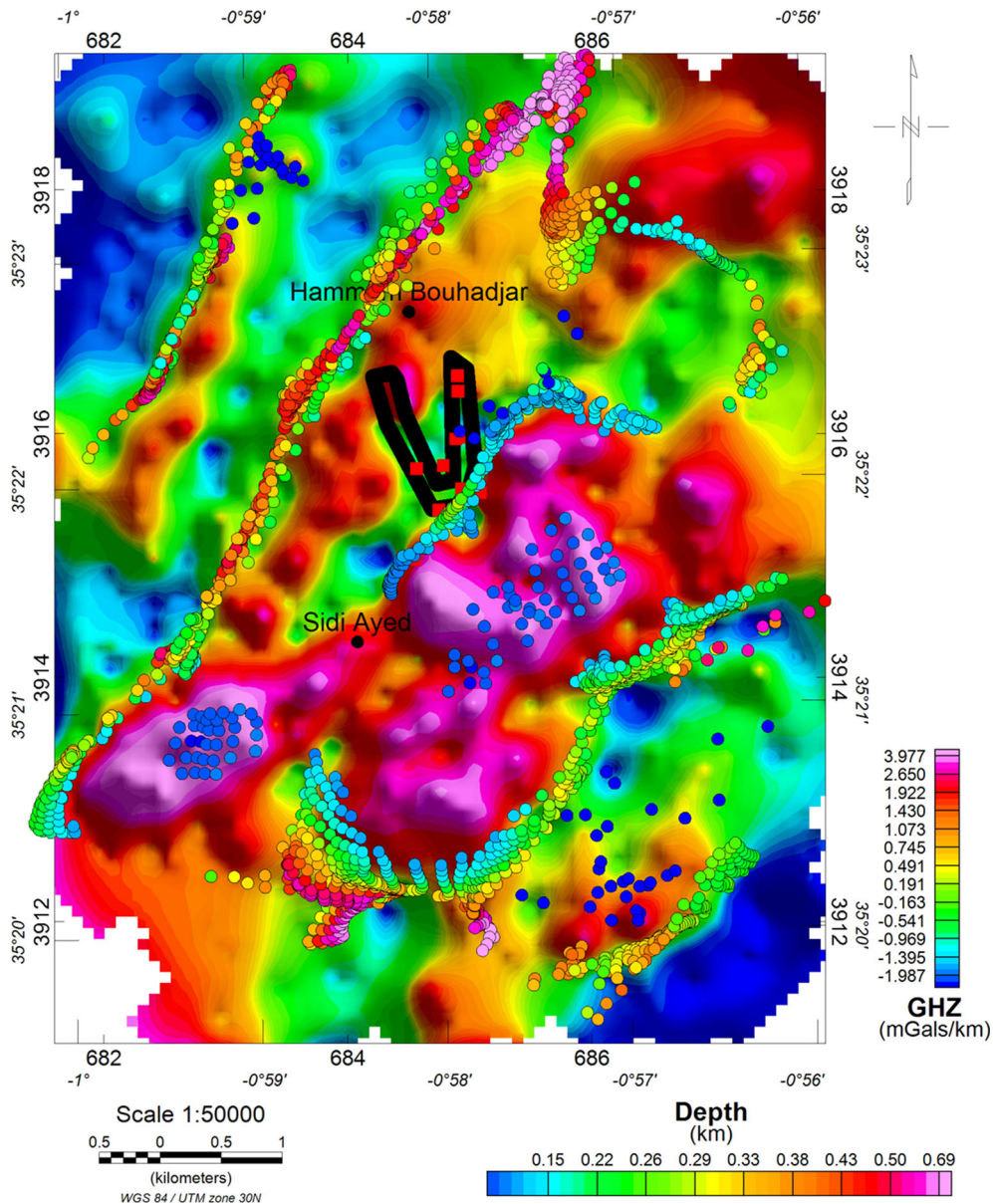


Figure 9

Euler solutions superimposed on the vertical gradient gravity map. These solutions were calculated with structural index = 0, window size = 12 and tolerance = 15%

*On Pliocene formation, located at the West of the Hammam Bouhadjar faults* It is clear that the second layer determined by this sounding corresponds to marls because of its very low resistivity (Fig. 11b).

*At the centre of volcanic emissions* The electrical sounding confirms the high resistivity formations (>30  $\Omega$ .m). These formations overcome a very thick

layer (probably 100 m) of  $\sim 15 \Omega$ .m resistivity (Fig. 11c) which correspond to clays.

#### 4.3.2 Geo-electrical Models

Located to the west of the studied area, the first geo-electrical section (P1 in Fig. 12a) shows resistant



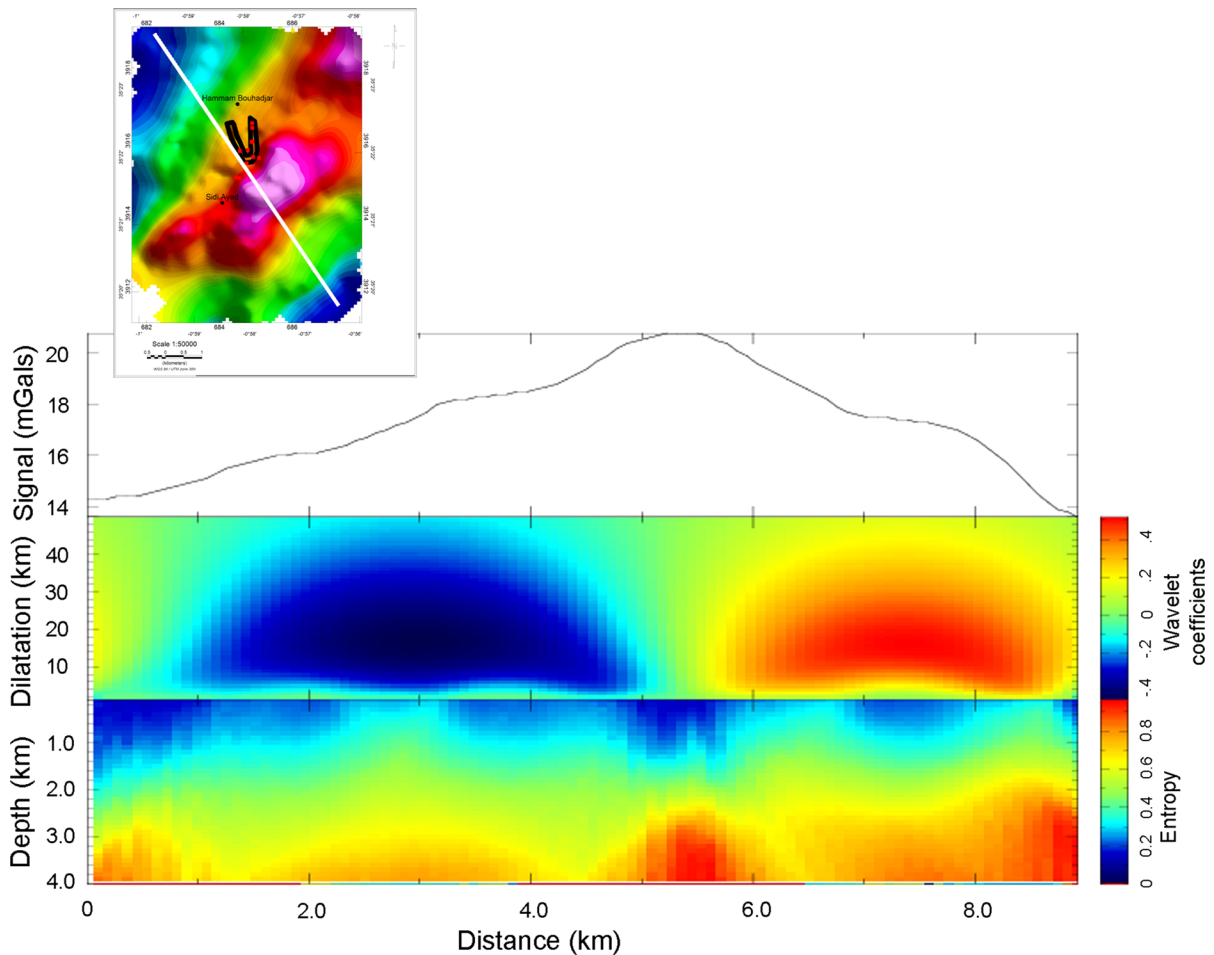


Figure 10

Identification of complete Bouguer gravity anomalies causative bodies using the continuous wavelet transform along NW-SE profile crossing the anomaly A2 (white line in square at the top left of the figure). The top of the figure shows the Bouguer gravity anomaly profile, the middle shows the coefficients of the wavelet transform and the bottom the maximum entropy map giving the depth of identified structures

surface layer whose thickness varies from 0.5 to less than 2 m (and sometimes more) (Fig. 12b). Here, the resistivity varies from 45  $\Omega$ .m and reaches the maximum of 200  $\Omega$ .m at SEV10. This layer constitutes the ground (or agricultural land) which is more resistive than in depth, probably due to the climatic conditions.

At the North of the profile appears a layer with a resistivity ranging from 12 to 19  $\Omega$ .m. It would correspond to clays.

Then, the layer whose thickness increases from South to North varies from 10 m in the South to about 200 m in North. Here, the resistivity is generally less than 6  $\Omega$ .m; it probably corresponds

to an essentially marls formation or clays with high concentration of more conductive material such as gypsum. This layer is clearly affected by step faults system (Fig. 12b). In sum, Electrical soundings have reached layer of resistivity between 10 and 15  $\Omega$ .m which is probably a clay formation that reaches the depth of 200 m and more.

A second geo-electrical section (P2 in Fig. 12a), located at the East of the studied area, shows faults, more clearly than in the first geo-electrical section, with a less important shift (Fig. 12c). In addition to the superficial surface layer, this section shows a continuous layer mainly of clays (resistivity between 10 and 20  $\Omega$ .m). The central part of profile is

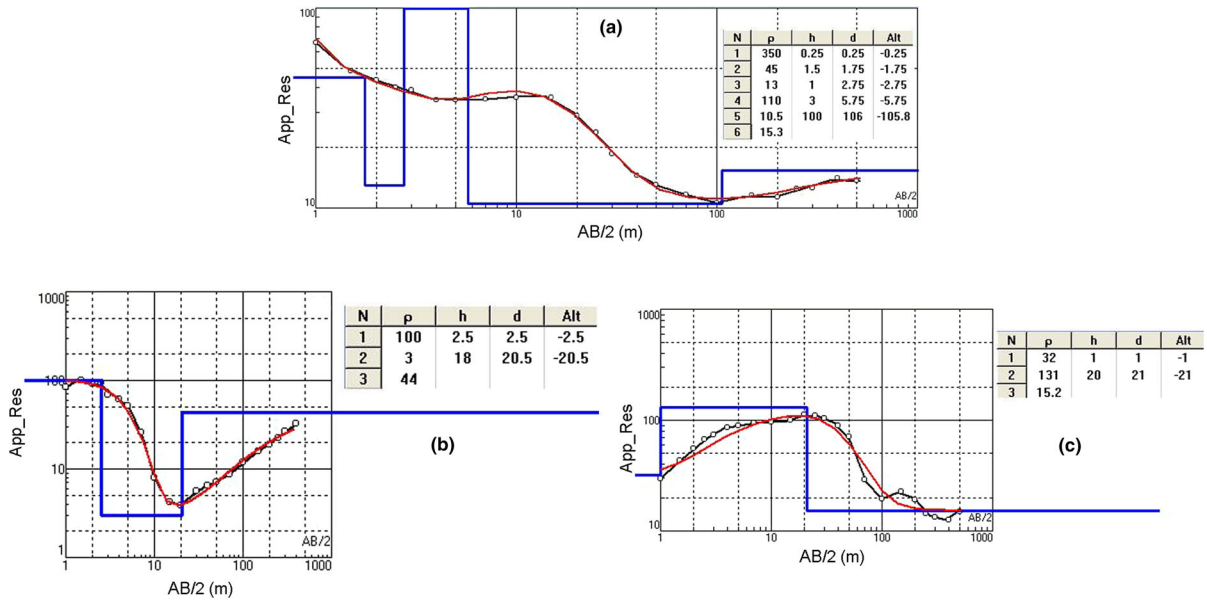


Figure 11

Calibration soundings. **a** At Hammam Bouhadjar drilling, **b**: on Pliocene formation and **c** at the centre of volcanic emissions. In each case, the *black curve* shows the resistivity measurement during the electrical prospecting and the red curve represents the resistivity calculated from inversion process. The table of each window shows the results from the inversion

characterized by a layer with resistivity equal to  $40 \Omega \cdot \text{m}$ , whose extension to the North cannot be confirmed. Indeed, if it is thin and lies between two conductor layers, the electrical prospecting is “blind” in this case. Reviewing the Hammam Bouhadjar drilling, this layer would be composed by limestone gravels to sandstone. The deepest layer which is imaged by the electrical prospecting is a conductive layer, presenting a resistivity less than  $10 \Omega \cdot \text{m}$ , and would be marls.

### 5. Origin of the Hammam Bouhadjar Thermal Waters

The Hammam Bouhadjar thermalism is noticeable by springs located at the fissures. These travertines were deposited by the flows of these hot springs (thermo-mineral) loaded by carbonates via with fractures and faults affecting the area. The thermal waters are ranging from cold to hyperthermal through hypothermal and mesothermal stages, with temperature variations from cold spring ( $9.5 \text{ }^\circ\text{C}$ ) to very hot spring ( $68.5 \text{ }^\circ\text{C}$ ) (Tabet Helal and Baghli 2005; Belhai

et al. 2014). Considering normal geothermal gradient of  $1 \text{ }^\circ\text{C}$  for 30 m and energy dissipation related to the upwelling, this water comes from depths exceeding 1000 m (e.g. water temperature Hammam Bouhadjar =  $61 \text{ }^\circ\text{C}$ , Sidi Ayed =  $56 \text{ }^\circ\text{C}$ ).

The majority of water sources present low flow to null. The only interested flows are those currently exploited: Hammam Bouhadjar (thermal complex), Sidi Ayed and El Hamda (Fig. 13). The PH is almost constant for all water sources; its variations ranges from 5.4 to 6.86 (Tabet Helal and Baghli 2005). The acid PH is due to the dissolved  $\text{CO}_2$  in the water coming from depths, and which reappears as gas bubble at emergence. This acid PH makes aggressive water, which dissolves the carbonates on its way. The analysis showed (constancy of the physicochemical values) that all these waters would have one origin, because they present the same facies and identical classification—Chloride sodic (Tabet Helal and Baghli 2005). This similarity shows that these waters have crossed eventually the same geological deposits.

It is likely that the origin of the hot springs of Hammam Bouhadjar baths is explained by the presence of these apophysis. Clearly, the thermal

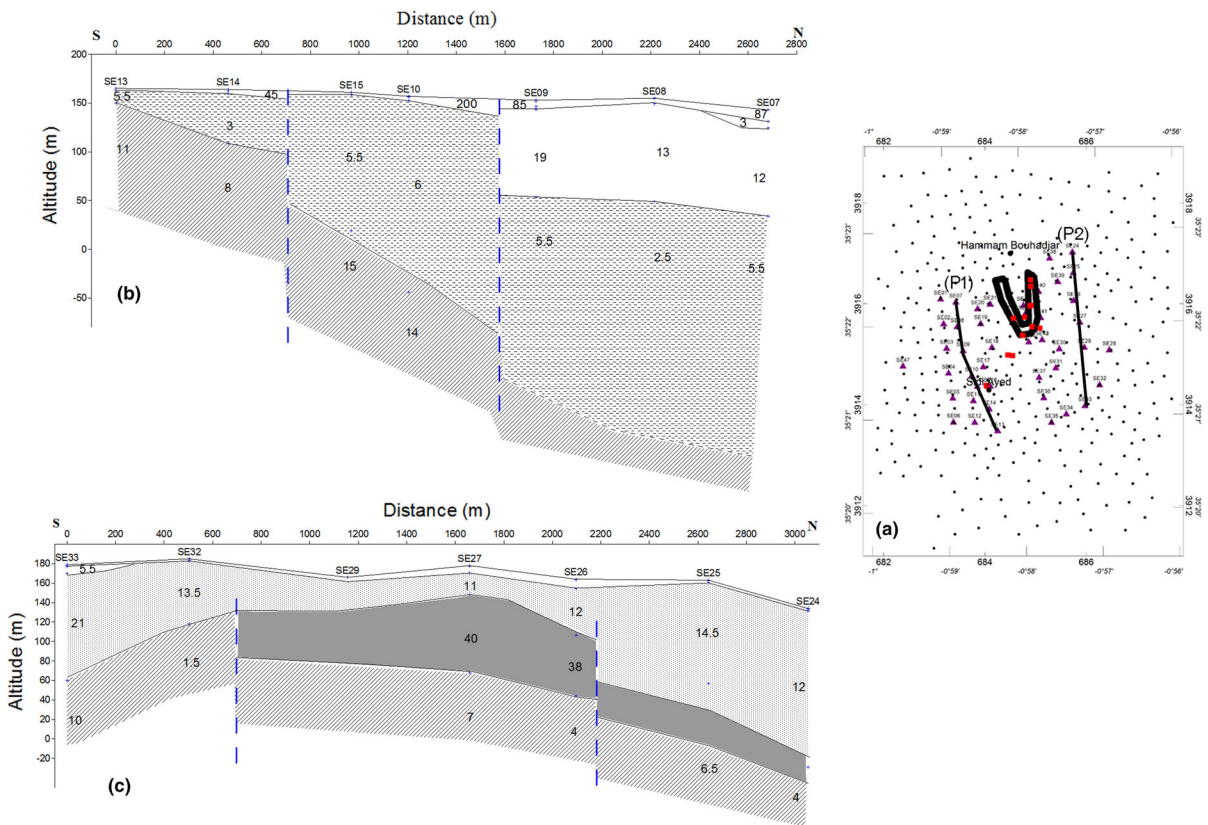


Figure 12

Geo-electrical models. **a** On the geophysical dataset map are located the geo-electrical sections P1 and P2 with *black lines* (*black circles* represent gravimetric measurements; *purple triangles* show electrical soundings; *red square* represents hot springs and the *black line* shows the travertine deposits, drawing the “horseshoe”). **b** Shows vertical and horizontal variations of resistivity along the geo-electrical section P1. **c** Shows vertical and horizontal variations of resistivity along the geo-electrical section P2. Clearly faults are identified (*blue dotted lines*) with more important shift in (**b**)

Hammam Bouhadjar waters are either related to deep warming of water table trapped in parautochthonous because of the geothermal gradient, or from another aquifer located above in the thrust Telliian unit (allochthonous), which would be warmed by the vicinity of one or many apophysis connected to an active magma chamber rooted deep under the parautochthonous. An aquifer located in the parautochthonous substratum brings at surface waters with variable composition where the dissolved minerals come from all geological sets crossed during their ascension. That is to say, the waters of this type contain minerals from du substratum and Telliian unit overlying.

In the studied area, the geophysical data set presented above bring new constraints to explain the

structural architecture of the hydrothermal system in Hammam Bouhadjar. The interpretation of results suggests strongly that the overall device articulates around collapse in the same place of the travertine walls, delineating the horseshoe of Hammam Bouhadjar. The faults responsible for this collapse have played in dextral way, causing failovers of blocs which are delimited and connected to the main fault of Oued el Melah (Fenet 1975).

These faulted structures, as we have shown, have been active contemporaneously with the volcanism visible in the area. The thermal waters spurt through the tension slots that accompanied the dextral movement of these faults. The water composition shows that they come from the same aquifer (Tabet Helal and Baghli 2005). This constraint allows saying that these waters

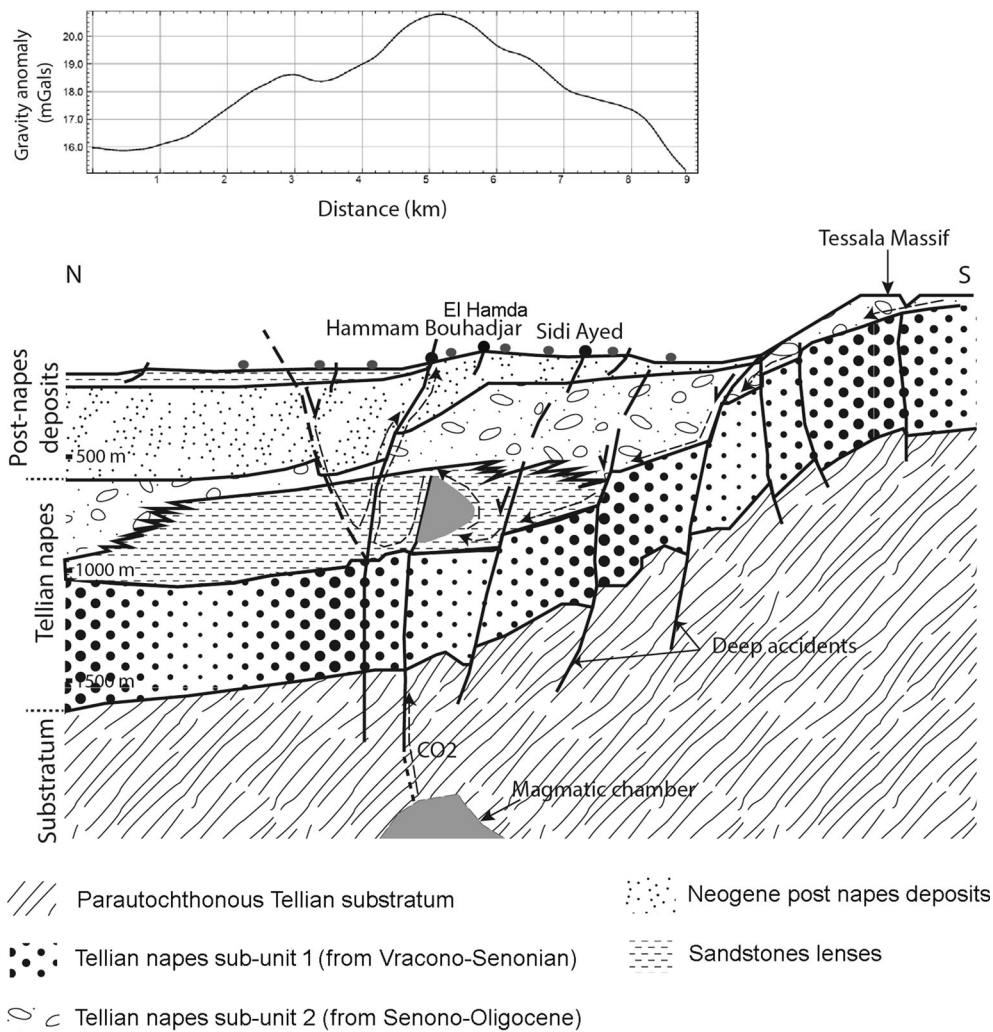


Figure 13

Synthetic scheme explaining the origin of the Hammam Bouhadjar thermal waters. The different faults and accidents shown by geophysical data are represented on the model. On the surface, the *black circles* show the hot springs and those in grey represent the electrical soundings position. In depth, the magmatic chamber and its upper apophysis are represented in grey. Following the gravity modelling the apophysis is located at about 800 m depth, while the chamber magmatic could not be imaged. *Upper panel*: measured gravity anomaly

do not originate from parautochthonous Tellian substratum and do not also originate from the limestone-carbonated Tellian unit (Vracono-Senonian), located above the parautochthonous. In this case, we make the assumption that the hot spring water will come from an aquifer located in sandstone lenses in the Senono-Oligocene Tellian unit, which overcomes the Vracono-Senonian unit cited above.

In these circumstances, following the gravity modelling, the aquifer is located at about 800 m, the same depth where the geothermal gradient is

insufficient to heat the water. The only possibility in agreement with these geological observations would be that the aquifer is heated by volcanic processes probably connected with hot compartment. The depth and the volcanism age (relatively young) dated to 0.82 Ma (Louni-Hacini et al. 1995; Coulon et al. 2002; Belhai et al. 2015) indicate that its energy has not completely dissipated. Therefore, it participates in the heating of the deep water.

The electrical modelling emphasizes the different superficial tectonic accidents. It also shows the



presence of conductor body along the horseshoe area. In depths greater than 400 m, this conductor is identified in the South part of the horseshoe. This observation indicates that the water percolates into this area and then is drained by different accidents to invade the whole area.

All these results allow us to propose a synthetic scheme or model (Fig. 13) of the spatial distribution of all elements that play roles in the thermal spring of Hamma Bouhadjar.

### 6. Conclusion

For the first time, gravity and electrical surveys are conducted in Hammam Bouhadjar area. This area is interesting because of its tectonic context with the containment of hydrothermal, travertines, ground-water and faults.

The main results we obtain are summarized as follows:

- The identification and localisation of faults and lineaments both near surface and at depth by the use of different processing methods of gravity field interpretation (gradients, upward continuation, Euler deconvolution, wavelet transform and gravity modelling).
- The presence of a conductor along of the horseshoe area suggests that the water percolates into this area and then is drained by the different accidents to invade the whole area.
- Following the gravity modelling the aquifer is identified at about 800 m, the same depth where the geothermal gradient is insufficient to heat the water.
- The aquifer is probably heated by volcanic processes connected with a hot compartment by faults and contacts affecting structures identified in depth.

### Acknowledgements

This work was supported by CRAAG (Centre de Recherche en Astronomie, Astrophysique et Géophysique). The authors are grateful to Dr. A. Yelles-Chaouche (CRAAG) and A. Bougrine (CRAAG) for different discussions. We also thank the editor and

the reviewers for their constructive remarks and comments.

### REFERENCES

- Abbassene, F., Chazot, G., Bellon, H., Bruguier, O., Ouabadi, A., Maury, R. C., et al. (2016). A 17 Ma on set for the post-collisional K-rich calc-alkaline magmatism in the Maghrebides: Evidence from Bougaroun (northeastern Algeria) and geodynamic implications. *Tectonophysics*, 674, 114–134. doi:10.1016/j.tecto.2016.02.013.
- Abtout, A., Boukerbout, H., Bouyahiaoui, B., & Gibert, D. (2014). Gravimetric evidences of active faults and underground structure of the Chelif seismogenic basin (Algeria). *Journal of African Earth Sciences*, 99, 363–373. doi:10.1016/j.jafrearsci.2014.02.011.
- Baranov, V. (1953). Calcul du gradient vertical du champ de gravité ou du champ magnétique mesuré à la surface du sol. *Earth Sciences, Geophysical Prospecting*, 1(3), 171–191.
- Belantour, O. (2001). Le magmatisme miocène de l'Algérois : chronologie de mise en place, pétrologie et implications géodynamiques. Thèse de doctorat, USTHB, Alger.
- Belhai, M., Fujimitsu, Y., Bouchareb-Haouchine, F.Z., Iwanaga, T., Noto, M. (2014). Geochemistry of the North Western Algerian Geothermal System. In Proceedings, Thirty-Ninth Workshop on Geothermal Reservoir Engineering Stanford University, Stanford, California, February 24–26, 2014 SGP-TR-202.
- Belhai, M., Fujimitsu, Y., Bouchareb-Haouchine, F.Z., Nishijima, J. (2015). Geology, geothermometry, isotopes and gas chemistry of the Northern Algerian geothermal system. In Proceedings, World Geothermal Congress. Melbourne, Australia, April 19–25.
- Benouar, D., Aoudia, A., Maouche, S., & Meghraoui, M. (1994). The 18 August 1994 Mascara (Algeria) earthquake; a quick-look report. *Terra Nova*, 6, 634–638.
- Bouillin, J.-P. (1986). Le "bassin maghrébin": une ancienne limite entre l'Europe et l'Afrique à l'ouest des Alpes. *Bulletin de la Société géologique de France*, 8(4), 547–558.
- Boukerbout, H., Gibert, D., & Sailhac, P. (2003). Identification of sources of potential fields with the continuous wavelet transform: Application to VLF data. *Geophysical Research Letter*, 30(8), 1427. doi:10.1029/2003GL016884.
- Bouyahiaoui, B., Djeddi, M., Abtout, A., Boukerbout, H., Akacem, N. (2011). Étude de la croûte archéenne du môle In Ouzzal (Hoggar Occidentale) par la method gravimétrique: identification des sources par la transformée en ondelettes continue, Bulletin de Service Géologique National. N°22, P259–274.
- Bracène, R., & Frizon de Lamotte, D. (2002). The origin of intraplate deformation in the Atlas system of western and central Algeria: from Jurassic rifting to Cenozoic-Quaternary inversion. *Tectonophysics*, 357, 207–226.
- Coulon, C., Megartsi, M., Fourcade, S., Maury, R. C., Bellon, H., Louni-Hacini, A., et al. (2002). Post-collisional transition from calco-alkaline to alkaline volcanism during the Neogene in Oranie (Algeria): magmatic expression of a slab break off. *Lithos*, 62, 87–110.
- Durand-Delga, M., & Fontboté, J. (1980). Le cadre structural de la Méditerranée occidentale, Mémoire. *BRGM*, 11, 65–85.
- Fedi, M., Premicieri, R., Quarta, T., & Villani, A. V. (2004). Joint application of continuous and discrete wavelet transform on

- gravity data to identify shallow and deep sources. *Geophysical Journal International*, 156, 7–21. doi:10.1111/j1365-246X.2004.02118.x.
- Fenet, B. (1975). Recherche sur l'alpinisation de la bordure septentrionale du bouclier africain, à partir de l'étude d'un élément de l'orogène nord maghrébin : les Monts du Djebel Tessala et les Massifs du littoral oranais. Thèse Doc Es Sci. Université de Nice.
- Frizon de Lamotte, D., Saint Bezar, B., Bracène, R., & Mercier, E. (2000). The two main steps of the Atlas building and geodynamics of the western Mediterranean. *Tectonics*, 19(4), 740–761.
- Gibert, D., & Galdeano, A. (1985). A computer program to perform transformations of gravimetric and aeromagnetic survey. *Computers & Geoscience*, 11, 553–588.
- Guardia, P. (1975). Géodynamique de la marge alpine du continent africain d'après l'étude de l'Oranie nord occidentale. Relations structurales et paléogéographiques entre le Rif externe, le Tell et l'avant-pays atlasique. Thèse Doc Es Sci. Université de Nice. N° A.O.11 417.
- Hornby, P., Boschetti, F., & Horovitz, F. G. (1999). Analysis of potential field data in the wavelet domain. *Geophysical Journal International*, 137, 175–196.
- Issaadi, A. (1996). Mécanismes de fonctionnement des systèmes hydrothermaux Application aux eaux thermo-minérales algériennes et aux eaux de Hammam Bou-Hadjar. *Bulletin du Service Géologique de l'Algérie*, 7(1), 71–85.
- Keller, G. V. (1966). Dipole method for deep resistivity studies. *Geophysics*, 31(6), 1088–1104. doi:10.1190/1.1439842.
- Loke, M. H., & Barker, R. D. (1996). Practical techniques for 3D resistivity surveys and data inversion. *Earth Sciences, Geophysical Prospecting*, 44(3), 499–523.
- Louni-Hacini, A., Bellon, H., Maury, R. C., Megartsi, M., Coulon, C., Belkacem, S., et al. (1995). Datation 40 K–40Ar de la transition du volcanisme calco-alcalin au volcanisme alcalin en Oranie au Miocène supérieur. *Comptes Rendus de l'Académie des Sciences Paris*, 321, 975–982.
- Maouche, S., Meghraoui, M., Morhange, C., Belabbes, S., Bouhadad, Y., & Haddoum, H. (2011). Active coastal thrusting and folding, and uplift rate of the Sahel Anticline and Zemmouri earthquake area (Tell Atlas, Algeria). *Tectonophysics*, 509(1–2), 69–80.
- Maury, R. C., Fourcade, S., Coulon, C., El Azzouzi, M., Bellon, H., Coutelle, A., et al. (2000). Post-collision neogene magmatism of the Mediterranean Maghreb margin: a consequence of slab Breakoff. *Comptes Rendus de l'Académie des Sciences Paris*, 331, 159–173.
- Megartsi, M. (1985). Le volcanisme mio-plio-quadernaire de l'Oranie Nord occidentale. Thèse Doc. Etat, U.S.T.H.B, Alger, 296 p.
- Meghraoui, M. (1988). Géologie des zones sismiques du Nord de l'Algérie. Paléosismologie, Tectonique Active et Synthèse sismotectonique, Thèse de Doctorat d'Etat, Université de Paris-Sud Orsay, pp 355.
- Meghraoui, M., & Doumaz, F. (1996a). Earthquake-induced flooding and paleoseismicity of the El Asnam, Algeria, fault-related fold. *Journal of Geophysical Research*, 101, 17, 617–17,644.
- Meghraoui, M., Morel, J. L., Andrieux, J., & Dahmani, M. (1996). Néotectonique de la chaîne Tello-Rifaine et de la Mer d'Alboran: une zone complexe de convergence continent-continent". *Bulletin de la Société Géologique de France*, 167, 143–159.
- Mikhailov, V., Galdeano, A., Diament, M., Gvishiani, A., Agayan, S., Bogoutdinov, S., et al. (2003). Application of artificial intelligence for Euler solutions clustering. *Geophysics*, 68, 168180. doi:10.1190/1.1543204.
- Moreau, F., Gibert, D., Holschneider, M., & Saracco, G. (1997). Wavelet analysis of potential fields. *Inverse Problems*, 13, 165–178.
- Oldham, C. W., & Sutherland, D. B. (1955). Orthogonal polynomials: their use in estimating the regional effect. *Geophysics*, 20, 295–306.
- Perrodon, A. (1957). Étude géologique des bassins néogènes sublittoraux de l'Algérie occidentale. Service de la Carte Géologique de l'Algérie (Nouvelle Série), Bulletin N° 12. 368p.
- Reid, A. B., Allsop, J. M., Granser, H., Millett, A. J., & Somerton, I. W. (1990). Magnetic interpretation in three dimensions using Euler deconvolution. *Geophysics*, 55(1), 80–91.
- Sailhac, P., Gibert, D., & Boukerbout, H. (2009). The theory of the continuous wavelet transform in the interpretation of potential fields: a review. *Geophysical Prospecting*, 57(4), 517–525.
- Savelli, C. (2002). Time-space distribution of magmatic activity in the western Mediterranean and peripheral orogens during the past 30 Ma (a stimulus to geodynamic considerations). *Journal of Geodynamics*, 34(1), 99–126. doi:10.1016/S0264-3707(02)00026-1.
- Spector, A., & Grant, F. S. (1970). Statistical models for interpreting aeromagnetic data. *Geophysics*, 35, 293–302.
- Tabet Helal, A., & Baghli, A. (2005). Étude hydrogéologique, hydrologique & hydrochimique, p 42-76. In Étude hydrogéologique de la zone thermique de hammam bouhdjar. Rapport interne, commune de Hammam Bouhadjar, 119 p.
- Thompson, D. T. (1982). EULDPH: A new technique for making computer-assisted depth estimates from magnetic data. *Geophysics*, 47, 31–37.
- Yelles-Chaouche, A. K., Djellit, H., Beldjoudi, H., Bezzeghoud, M., & Buforn, E. (2004). The Ain Temouchent (Algeria) earthquake of December 22nd, 1999. *Pure and Applied Geophysics*, 161(3), 607–621.